The effect of κ-carbides on high cycle fatigue behavior of a Fe-Mn-Al-C lightweight steel

Gomez, A.; Banis, A.; Avella, M.; Molina-Aldareguia, J. M.; Petrov, R. H.; Dutta, A.; Sabirov, I.

DOI
10.1016/j.ijfatigue.2024.108306

Publication date
2024

Document Version
Final published version

Published in
International Journal of Fatigue

International Journal of Fatigue 184 (2024) 108306

Contents lists available at ScienceDirect

International Journal of Fatigue

journal homepage: www.elsevier.com/locate/ijfatigue

The effect of κ-carbides on high cycle fatigue behavior of a Fe-Mn-Al-C lightweight steel

A. Gomez [a], A. Banis [b], M. Avella [a], J.M. Molina-Aldareguia [c,a], R.H. Petrov [b,e], A. Dutta [d], I. Sabirov [a,*]

[a] IMDEA Materials Institute, Getafe, Madrid, Spain
[b] Department of Electromechanical, Systems and Metal Engineering, Ghent University, Ghent, Belgium
[c] Department of Mechanical Engineering, Universidad Politécnica de Madrid, José Gutiérrez Abascal, 2, Madrid 28006, Spain
[d] ArcelorMittal Global R&D, Ghent, Belgium
[e] Materials Science and Engineering Department, Faculty ME, Delft University of Technology, Delft, the Netherlands

ARTICLE INFO

Keywords:
Lightweight steel
Fatigue
Quasi-cleavage
Crack
κ-carbides

ABSTRACT

Numerous studies have demonstrated the viability of lightweight Fe-Mn-Al-C steels for exhibiting an improved balance of high strength and high ductility in automotive applications. However, their high-cycle fatigue behaviour has been scarcely studied. This work examines the effect of κ-carbides formed during the aging treatment on the high-cycle fatigue performance of an austenitic Fe-29Mn-8.7Al-1C (wt. %) steel. The material is studied in solution-treated, under-aged, and peak-aged conditions. High-cycle fatigue tests and analysis of fatigue fracture surfaces were performed using SEM and EBSD techniques. The results indicate satisfactory high-cycle fatigue performance in the aged material, somewhat better than for high Mn steels. Fatigue crack formation and growth occur predominantly via a quasi-cleavage mechanism along the [1 1 1] crystallographic planes, which is also a plane for planar glide and the formation of persistent slip bands during plastic deformation. The nanoscale intragranular κ-carbides in the aged samples interact with the gliding dislocations, resulting in the shearing of nanoscale κ-carbides in a weakly coupled regime. The resistance of particles to shearing is determined by their size, volume fraction, and antiphase boundary energy (γ_{APB}), which vary during the aging process. The aged Fe-29Mn-8.7Al-1C steel significantly improves the fatigue strength as the formation of persistent slip bands is delayed due to an additional energy barrier related to the shearing of the κ-carbides. This improvement peaks in the under-aged condition and decreases with further aging time.

1. Introduction

Automotive engineers continually explore innovative approaches to achieve multiple goals, including reducing vehicle weight, lowering fuel consumption and related emissions, and enhancing overall performance and handling characteristics. For instance, a rough estimate suggests that emissions could be reduced by approximately 6.9 % for every 10 % reduction in vehicle weight. Consequently, engineers are increasingly focusing on lighter materials, such as aluminum, magnesium, titanium alloys, composites, and advanced high-strength steels (AHSSs).

Among these materials, lightweight steels have been developed as suitable for structural components and assemblies due to their exceptional combination of high strength and toughness [1]. The reduction of steel density is particularly advantageous, allowing for an increase of specific strength and a direct weight reduction of parts made of steel. Alloying elements with a lower density than Fe (7.8 g/cm^3), such as Al (2.7 g/cm^3), Si (2.3 g/cm^3) and Mn (7.21 g/cm^3) are added to Fe-C steels to reduce the density as well as to control the phase composition [2]. These light elements alter the lattice parameter of steels and simultaneously reduce density due to their low atomic masses. For example, a 12 (wt. %) Al addition will reduce the density of Fe by 17 % of which lattice dilatation contributes with 10 % and atomic mass reduction contributes with an additional 7 % [1]. The most widely studied steels of this family are based on the Fe-Mn-Al-C system and have recently attracted significant attention of the steel research community and various industries [1–3]. It has been demonstrated that processability, microstructure and properties of the Fe-Mn-Al-C steels strongly depend on chemistry, applied thermo-mechanical processing parameters and processing scale [1–3]. Their constitutive phases can be either ferrite,

* Corresponding author at: IMDEA Materials Institute, Calle Eric Kandel 2, Getafe, 28906, Madrid, Spain.
E-mail address: ilchat.sabirov@imdea.org (I. Sabirov).

https://doi.org/10.1016/j.ijfatigue.2024.108306
Received 15 January 2024; Received in revised form 14 March 2024; Accepted 26 March 2024
Available online 2 April 2024

Nomenclature

γ_{ABP}	Antiphase boundary energy
ε_f	Elongation to failure
σ_f	Fatigue strength
f	Frequency
σ_{max}	Maximum stress
R	Stress ratio
σ_{UTS}	Ultimate tensile strength
ε_U	Uniform elongation
σ_y	Yield strength
HV	Vickers hardness
AHSS	Advanced high-strength steels
BF	Bright field
DF	Dark field
EBSD	Electron backscatter diffraction
EDS	Energy dispersive X-ray spectroscopy
FCC	Face-centered cubic lattice
IFFT	Inverse Fast Fourier Transformation
HCF	High-cycle fatigue
HR	Hot-rolled
KAM	Kernel Average Misorientation
LCF	Low-cycle fatigue
ND	Normal direction
RD	Rolling direction
PA	Peak-aged
SEM	Scanning electron microscopy
SAED	Selected area electron diffraction pattern
SHT	Solution heat-treated
TEM	Transmission electron microscopy
TWIP	Twinning Induced Plasticity
TD	Transverse Direction
UA	Under-aged

Table 1
Chemical composition of the studied material (wt. %).

Element	Fe	Mn	Al	C	Si	P	S	Ti	Cu	Cr	O	N
Content	61.2	29.0	8.7	0.983	0.062	0.003	0.004	0.007	0.03	0.006	0.002	0.002

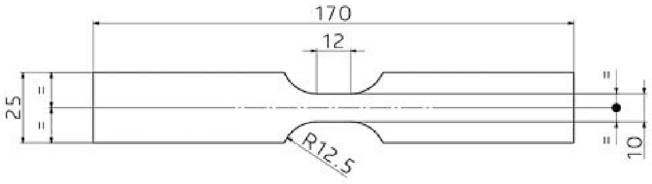

Fig. 1. The geometry of the fatigue specimens.

Table 2
Parameters of fatigue testing.

Parameter	Symbol	Values
Stress ratio	R	0.1
Frequency	f	30 Hz
Maximum stress	σ_{max}	360, 370, 380, 400, 440, 460, 470, 480, 490, 500, 510, 520, 540, 560, 600, 640, 680, 740, 760, 800 MPa
Minimum stress	σ_{min}	$\sigma_{min} = R \cdot \sigma_{max}$

austenite or a mixture of ferrite and austenite depending on the content of austenite stabilizing Mn and C and heat treatment parameters. Among this type of lightweight steels, the austenite-based Fe-Mn-Al-C steels show superior weight reduction effect and possess both high strength and ductility, which are closely associated with their unique microstructural features and deformation mechanisms. Additionally, they show a better processability [4]. A full austenitic structure at room temperature can be achieved in Fe-Mn-Al-C steels with high Mn and high C contents, falling within the range of 13–40 % and 0.6–2.0 %, respectively, despite the high-Al content [4]. Furthermore, austenitic steels demonstrate higher ductility and similar strength compared to duplex steels [2].

There is a significant body of experimental research focused on the microstructural design in austenitic Fe-Mn-Al-C steels to improve their mechanical properties. It has been well established that these steels possess favorable mechanical properties with a broad range for regulation, including yield strength (375–1850 MPa), ultimate tensile strength (765–1978 MPa), and total elongation (10–80 %) [4]. These properties vary depending on the chemistry and microstructure. The κ-carbides formed during heat treatment play a key role [5–13]. Coarse intergranular κ-carbides can lead to a sudden loss of elongation to failure, while fine intragranular κ'-carbides enhance the strength of lightweight steels without significantly sacrificing ductility [5–12]. Moreover, although the relationship between strength and ductility of duplex and single-austenitic lightweight steels follows the "banana" curve, the mechanical properties of austenitic steels with high-Mn content seem to be superior to those of duplex ones. The increase in Mn content appears to provide more room for improving the strength and ductility of steels, but it also raises challenges in fabrication, not to mention the increment in material cost [13].

The fatigue behavior of Fe-Mn-Al-C steels has been scarcely investigated, and due to limited amount of experimental data in the literature, it cannot be properly understood. High cycle fatigue behaviour of three solution-treated Fe-29Mn-9Al-(0.26, 0.6, 1.06)C (wt. %) alloys was studied in [14]. The volume fraction of austenite increased with increasing carbon content from 45 % to 100 %. No significant effect of austenite volume fraction on fatigue life was found, while strength increased with the increasing austenite content. The effect of aging treatment on the low cycle fatigue of an austenitic Fe-29.7Mn-8.7Al-1C alloy was studied in [15]. Cyclic softening was observed during fatigue for all aging conditions, which was related to the planar slip, shearing of kappa-carbides, mechanical dissolution of the precipitates, or formation of persistent slip bands depending on the aging condition. Kalashnikov et al. [16] investigated fatigue at a constant strain amplitude on a wrought Fe-28Mn-9Al-0.86C-0.7 W-0.43Mo-0.49Nb (wt. %) alloy and on a martensitic stainless steel of composition Fe-12Cr-1.25Ni-0.2 V-1.8 W-0.5Mo-0.15C. Three tests were conducted at different temperature conditions: one test at 400 °C, a second at 20 °C and a third test that included cycling the temperature between 400 and 20 °C. In each case, the stainless steel failed at half the cycles of the Fe-Mn-Al-C alloy. Tempering of the martensite and loss of strength were used to explain the lower cyclic life of the stainless steel at elevated temperatures. Wegener et al. [17] studied microstructure evolution and mechanical behavior of a Fe-29.8Mn-7.65Al-1.11C (wt. %) lightweight steel under strain controlled cyclic loading in the low-cycle fatigue (LCF) regime.

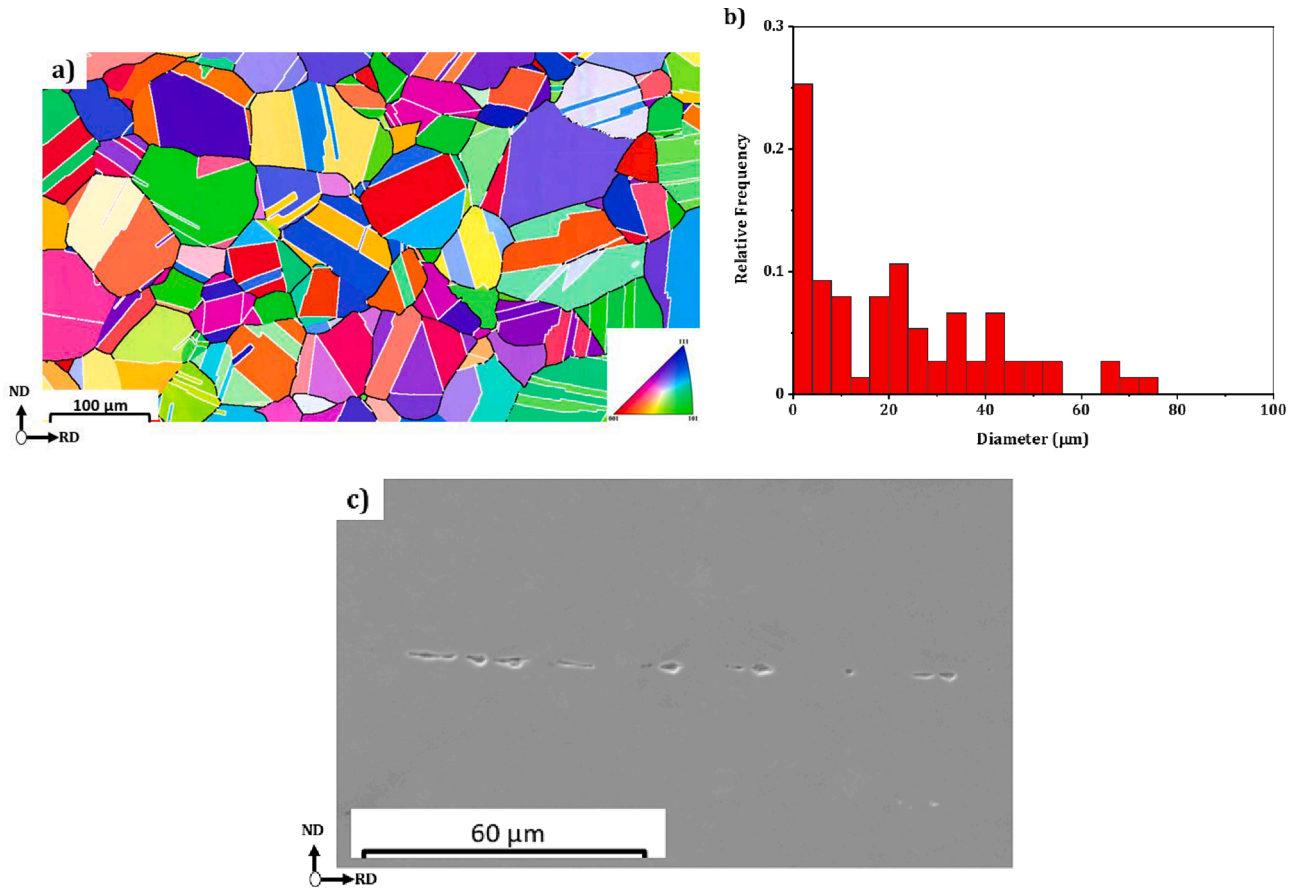

Fig. 2. a) IPF Y EBSD map of the solution heat treated sample; b) histogram of grain size distribution; c) MnS inclusions present in the microstructure. The twin boundaries <111>60° are marked by white lines on Fig. 2a.

The material was studied in two conditions: solution treated (without κ-carbides) and solution treated and aged (containing κ-carbides). It was found that the cyclic deformation response of the solution treated condition was characterized by initial cyclic softening followed by a stress plateau. However, aging modified the response dramatically. For the lowest total strain amplitude (±0.2 %), κ-carbides improved LCF performance. The increasing strain amplitude led to cyclic softening resulting in inferior fatigue life as compared to the solution treated samples. The latter phenomenon was related to the shearing of κ-carbides and mechanical dissolution of the precipitates during plastic deformation.

The high cycle fatigue behavior of Fe-Mn-Al-C steels was studied even to lesser extent. In [18], the high cycle fatigue performance of high-Mn austenitic steels was investigated at 298 and 110 K. It was shown that tensile strength was the most important parameter in determining the resistance to high cycle fatigue of high-Mn steels. The fatigue crack initiated via grain boundary cracking. Temperature did not affect the mechanisms of the fatigue crack initiation. The effect of κ-carbides on the high cycle fatigue behavior of Fe-Mn-Al-C steels still remains a white spot. The main objectives of this work are to explore the effect of κ-carbides on the high cycle fatigue resistance of a Fe-29Mn-8.7Al-1C (wt. %) steel and to unravel the mechanisms of fatigue crack initiation and growth.

2. Experimental procedures

2.1. Material and heat treatments

The Fe-29Mn-8.7Al-1C (wt. %) alloy was produced for this study. The chemical composition of the material is provided in Table 1. The content of O, N, C, and S was measured by combustion analysis, while the remaining elements were measured using XRF technique. The material was initially provided in the form of hot-rolled strips with a thickness of approximately 5 mm. Upon receiving the material, various heat treatments were applied. In the first stage, it underwent a solution treatment at 1000 °C for 30 min, followed by quenching in water. This solution treatment was executed in a muffle furnace, with the samples embedded in a pre-heated bath filled with fine sea sand. The use of sand served the purpose of minimizing surface oxidation, ensuring a rapid heating rate, and maintaining precise temperature control during the heat treatment process. Subsequently, a portion of the samples underwent aging at 550 °C for two different durations: 1 h and 8 h, followed by quenching in water. The aging treatments were also conducted in the pre-heated bath. The sample aged for 1 h is designated as being in an under-aged (UA) condition, while the sample aged for 8 h is considered to be in the peak-aged (PA) condition. Henceforth, they will be referred to accordingly.

2.2. Microstructural characterization

Quantitative microstructural characterization of the material was conducted using electron backscatter diffraction (EBSD) analysis. Specimens underwent grinding (up to 2000 SiC/in^2) and polishing procedures (1 and 3 µm diamond paste suspension) following standard metallographic techniques to achieve a mirror-like surface. The final polishing was carried out using colloidal silica suspension (OPS-0.25 µm). The EBSD studies of the SHT material were performed on the plane of the sample that contains normal direction (ND or Y) and rolling direction (RD or X) using an APREO 2S LoVac equipped with an Oxford Instruments Symmetry S2 EBSD detector controlled by the AZtec Oxford

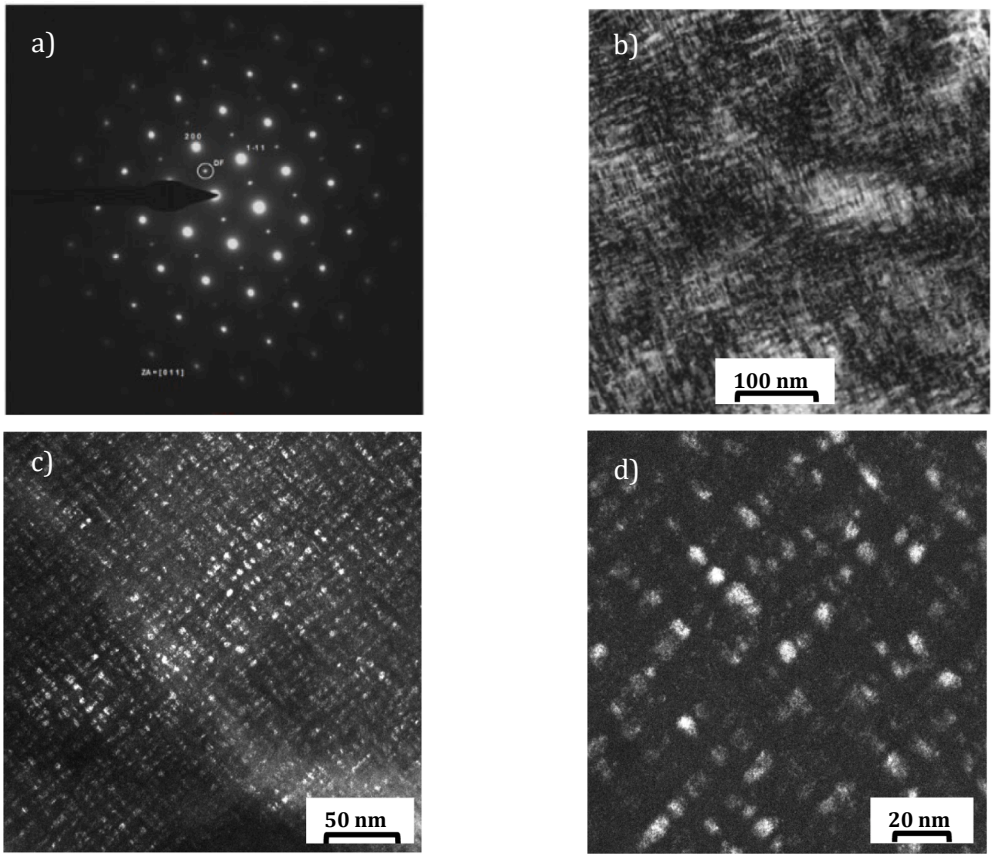

Fig. 3. a) SAED pattern of UA condition; b) BF TEM image; c) DF TEM image; d) DF TEM image at higher magnification.

Instruments Nanoanalysis (version 5.0) software. The data were acquired at an accelerating voltage of 20 kV, a working distance of 15 mm, a tilt angle of 70°, and a step size of 120 nm in a square scan grid. The orientation data were post-processed using HKL Post-processing Oxford Instruments Nanotechnology (version 5.12) software. The grain size was calculated using the grain definition of a minimum of 4 points per grain and a minimum misorientation of 15°. Local misorientations were used to estimate the strain localization in the microstructure. They were calculated using the Kernel average misorientation approach for the third nearest neighbor and maximum misorientation of 5°. A MATLAB code, developed by T.R. Bieler et al. [19], was utilized to identify the lattice planes associated with fatigue crack formation and growth based on the outcomes obtained from electron backscatter diffraction (EBSD).

The fracture surfaces of the fatigue specimens were examined using the scanning electron microscope EVO MA15 from Zeiss, operating at an accelerating voltage of 20 kV. Energy dispersive X-ray spectroscopy (EDS) analysis was carried out using the Oxford Instruments Ultim Max 40 detector to identify inclusions when necessary.

For a detailed investigation of the nanoscale κ-carbides formed in the material during aging, transmission electron microscopy (TEM) studies were performed using a FEG S/TEM (Talos F200X, FEI, and Jeol JEM-2200FS from Gent University), operated at an accelerating voltage of 200 kV. Thin foils were prepared on a TenuPol 5 (Struers®) through twin-jet electropolishing with a 10 % perchloric acid solution in acetic acid at room temperature and an operating voltage of 20 V. TEM imaging was acquired in bright-field (BF), dark-field (DF) and inverse fast Fourier transformation (IFFT) modes.

2.3. Mechanical characterization

Standard tensile samples with a gauge length of 50 mm and a gauge width of 12.5 mm were machined from the materials. Tensile tests were conducted using the INSTRON 3384 testing system following the ASTM E8 standard [20]. The tests were performed at room temperature, maintaining a constant cross-head speed of 2.5 mm/min. To ensure accurate measurement of deformation, an extensometer was affixed to the gauge section of each sample. At least three samples were tested for each condition, and the results were found to be reproducible. The average values are given.

The microhardness of the material was measured using SHIMADZU HMV-2 microhardness tester equipped with a Vickers diamond indenter. A load of 500 g was applied for 15 s. Ten measurements were carried out on each sample. The average values are presented.

Fatigue testing specimens were precision-machined from the heat-treated strips, with the geometric details illustrated in Fig. 1 below. The samples were machined in transverse direction (TD). Rigorous attention was given to the surface quality of the specimens, employing standard metallographic techniques. This meticulous preparation aimed to eliminate any superficial defects introduced during the machining process, as well as to remove oxide and demanganized layers formed during processing and heat treatments. Subsequent to the sample preparation, high-cycle fatigue tests were conducted under pull-pull stress-controlled conditions, employing sinusoidal-waveform cyclic loading. The experiments were carried out at room temperature using an INSTRON 8802 servohydraulic fatigue testing system, adhering to the ISO 1099 standard [21]. The stress ratio (R) was set at 0.1, and the load frequency (f) was maintained at 30 Hz. Recording the number of cycles to failure, S-N curves (Wohler curves) were constructed. A minimum of 14 samples were tested for each material, and the fatigue strength (σ_f) was estimated based on the resulting Wohler curves. It was defined as the highest maximum stress that a material can withstand for 10^7 cycles without breaking. The parameters of fatigue testing are summarized in Table 2.

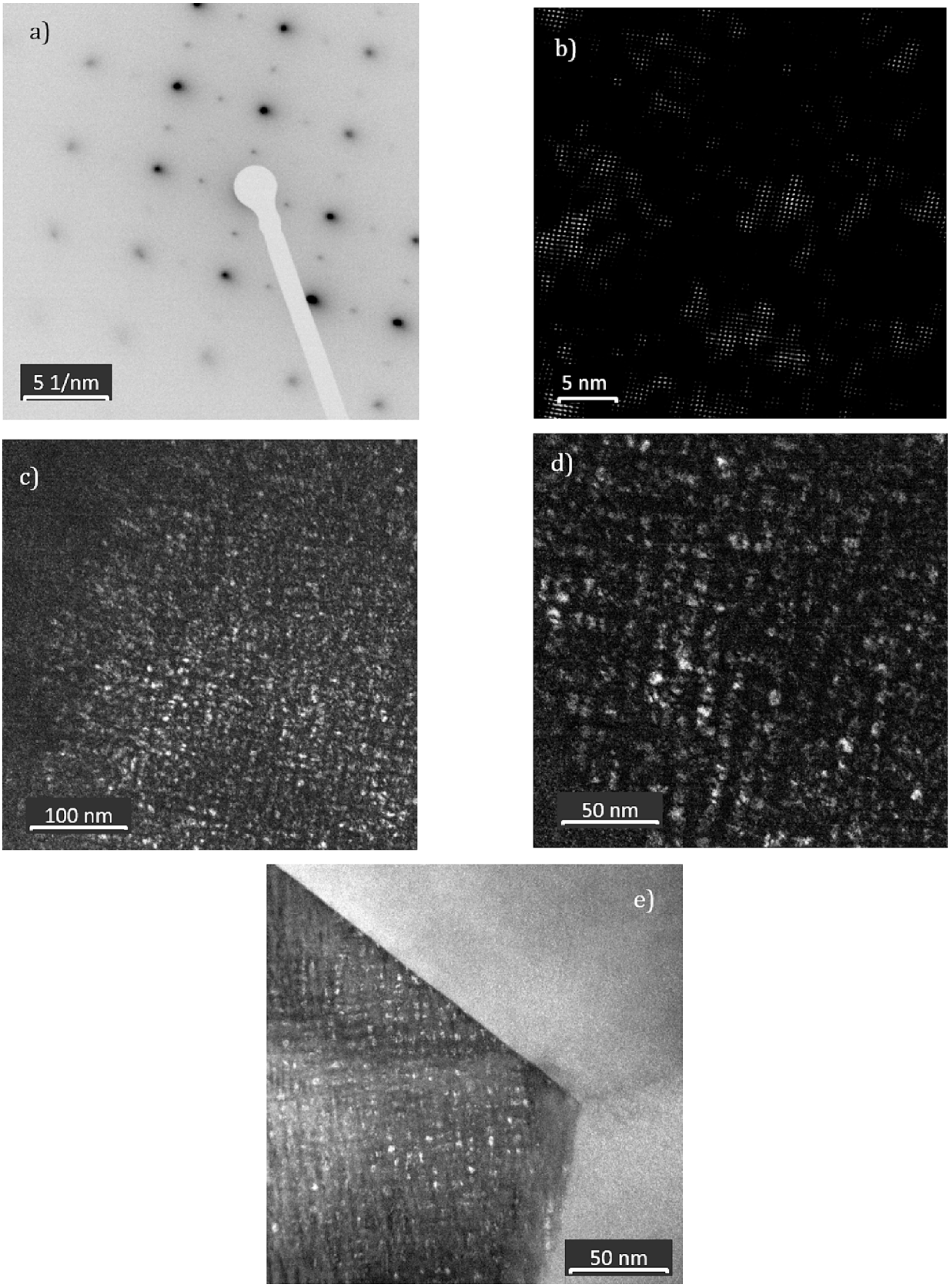

Fig. 4. a) SAED pattern of PA condition; b) high resolution TEM image of PA sample; c) DF TEM image at lower magnifications; d) DF TEM image at a higher magnification where the shape and distribution of κ-carbides are shown; e) No evidence of κ-carbides in grain boundary or triple junction area.

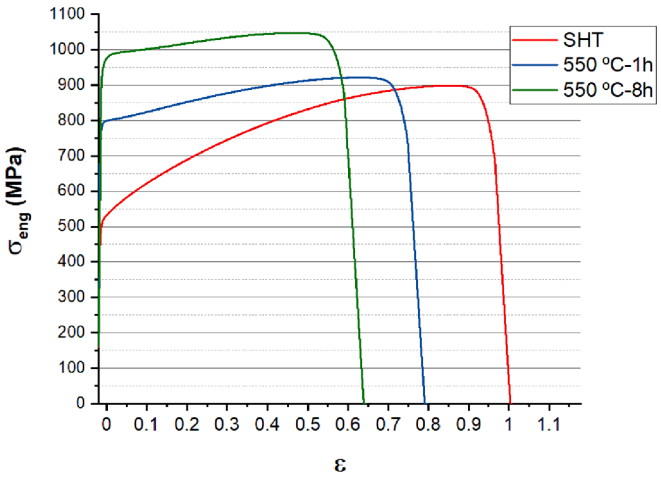

Fig. 5. Engineering stress – engineering strain curves obtained from tensile testing.

3. Results and discussion

3.1. EBSD analysis

The solution treated material exhibits a homogeneous austenitic non-textured microstructure with equiaxed grains (Fig. 2a). Most grains contain annealing twins. The histogram of grain size distribution is presented on Fig. 2b. The average grain size corresponds to 22.6 μm. Elongated MnS inclusions could also be observed in the microstructure (Fig. 2c). Although their volume fraction is negligibly low, these elongated MnS inclusions have a length up to 8 μm and a width up to 3 μm. They are typically present in steels [22]. Notably, the aging treatment at 550 °C did not alter the grain structure of the solution treated material. TEM analysis of the solution treated material did not reveal presence of any nanoscale κ-carbides in the microstructure.

3.2. TEM analysis of κ-carbides formed during the aging treatment

TEM was utilized to observe the nanoscale κ-carbides in the aged samples. Fig. 3a presents selected area electron diffraction (SAED) patterns from an austenite grain of the UA material oriented at zone axis of [0 1 1]. The large spots correspond to the fcc lattice of the austenitic matrix, while fine spots represent the κ-carbides. Nanoscale intragranular κ-carbides are clearly seen on the dark-field (DF) image of the austenitic grain (Fig. 3c). They have predominantly cuboidal shape and are homogeneously distributed over the grain (Fig. 3d). Quantitative characterization of the intragranular κ-carbides yields their average size of 3.1 ± 0.8 nm, and local volume fraction of 9.8 %. No intergranular κ-carbides are observed in the microstructure.

Fig. 4 illustrates nanoscale intragranular κ-carbides formed in the PA material. The analyzed grain is oriented at the zone axis at [0 0 1]. Spots corresponding to the austenitic matrix and κ-carbides can be easily identified on the SAED patterns (Fig. 4a). From the DF TEM image, it is clearly seen that cuboidal κ-carbides are homogeneously distributed over the grain (Fig. 4b-d). The increase of aging time results in slightly larger average κ-carbide size of 3.4 ± 1.0 nm. The local volume fraction of κ-carbides also increases to 10.7 %. It should be noted that longer aging time does not result in the formation of intergranular κ-carbides, as it was observed during aging treatment of the material at higher temperatures (650 °C) in [6,7]. Grain boundaries and triple junctions are free of κ-carbides as can be seen on Fig. 4e.

Table 3
Tensile and fatigue properties of the Fe-29Mn-8.7Al-1C alloy in solution heat treated, UA and PA conditions. Properties of high Mn steels from [18,19,23–29] are also provided for comparison.

Sample	Tensile properties						Fatigue properties	
	$\sigma_{0.2}$ [MPa]	σ_{UTS} [MPa]	$\sigma_{8\%}$ [MPa]	ε_u [%]	ε_f [%]	Hv	σ_f [MPa]	$\sigma_{max}/\sigma_{UTS}$
SHT	561	900	586	89	104	244	360	0.40
UA (550 °C/1h)	765	918	813	64	76	333	510	0.56
PA (550 °C/8h)	929	1060	995	41	54	384	460	0.43

Table 4
Tensile and fatigue properties of high Mn steels from literature [18,19,23–29].

Sample	Tensile properties			Fatigue properties					Ref.
	$\sigma_{0.2}$ [MPa]	σ_{UTS} [MPa]	ε_f [%]	Test Type	R	σ_a [MPa]	σ_{max} [MPa]	$\sigma_{max}/\sigma_{UTS}$	
3C16MnAl	268	830	98	Bending	−1	398	398	0.48	[23]
16Mn2Al0.3C	268	830	98	Bending	−1	358	358	0.43	[23,24]
16Mn2Al0.7C	494	951	72	Axial	0.1	191	424	0.45	[18,25,26]
6C18MnNb	308	963	91	Bending	−1	404	404	0.42	[23]
18Mn0.6C	410	1078	68	Axial	0.1	203	451	0.42	[29]
18Mn0.6C0.02Nb	308	963	91	Bending	−1	365	365	0.38	[23,24]
6C22Mn	316	866	96	Bending	−1	398	398	0.46	[23]
22Mn0.6C	316	866	96	Bending	−1	366	366	0.42	[23,24]
22Mn3Al3Si0.01C	353	812	94	Bending	−1	333	333	0.41	[24]
22Mn3Cr0.6C	462	1016	63	Axial	0.1	160	355	0.35	[18,27]
24Mn4Cr0.5C	499	982	72	Axial	0.1	208	462	0.47	[18,27]
25Mn	436	944	55	Axial	0.1	185	411	0.44	[19]
25Mn0.4C	436	944	55	Axial	0.1	130	289	0.31	[18,25]
25Mn0.5C0.2Al	457	988	52	Axial	0.1	150	333	0.34	[18]
25Mn0.2Al	457	988	52	Axial	0.1	175	389	0.39	[19]
25Mn0.5Cu	439	917	53	Axial	0.1	205	456	0.50	[19]
25Mn0.5Cu0.4C	439	917	53	Axial	0.1	159	353	0.39	[18]
30Mn0.9C	350	960	90	Axial	−1	250	250	0.26	[28]

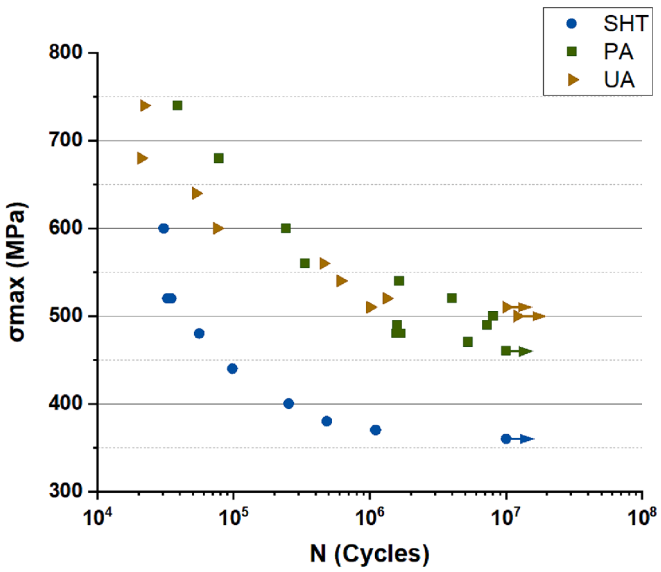

Fig. 6. Wöhler curves from high cycle fatigue testing.

3.3. Tensile testing

Engineering stress – engineering strain curves from tensile testing are presented in Fig. 5. The outcomes of their analysis are listed in Table 3. It is clearly seen that both yield strength and ultimate tensile strength increase with the increasing aging time, whereas uniform elongation, elongation to failure and strain hardening ability of the material show the opposite trend. It has been well established that the strength increase is related to precipitation strengthening induced by intragranular nanoscale κ-carbides during artificial aging (Fig. 3, Fig. 4) [5–12].

Microhardness testing of the studied material showed gradual increase with aging time from the solution heat treated condition to the peak-aged condition. These results are in a very good accordance with the outcomes of tensile testing. The Vickers hardness of work-hardening metallic materials HV follows the relationship HV ≈ $3{\cdot}\sigma$, where σ is the uniaxial tensile flow stress at plastic strain between 8 % and 10 % [30]. In our case, a linear correlation between HV and flow stress at 8 % is found with the coefficient of determination $R^2 = 0.99$ and linear coefficient of 3.1.

In Table 4, data from the mechanical properties characterization of various high-Mn steels reported in the literature [18,23–29] is gathered. A comparison of the tensile properties of our materials (Table 3) with those reported in the literature (Table 4) shows that the studied Fe-29Mn-8.7Al-1C alloy exhibits better yield and ultimate tensile strength compared to nearly all other high-Mn steels, while their tensile elongation to failure shows comparable values. As is widely recognized, the strength and ductility of steels are influenced by their chemistry and microstructure. The microstructure, in turn, is determined by both chemistry and process parameters. Given the significant variations in both chemistry and microstructure among the analyzed steels (Table 4), establishing a direct correlation between steel chemistry and tensile properties proves challenging.

3.4. Fatigue testing

Fig. 6 presents the *S–N* curves obtained from high cycle fatigue testing of the studied materials. The number of cycles, that the steels can endure before failure, tends to increase with decreasing stress amplitude. In general, the aged samples demonstrate much better fatigue resistance compared to the solution heat treated material. At maximum

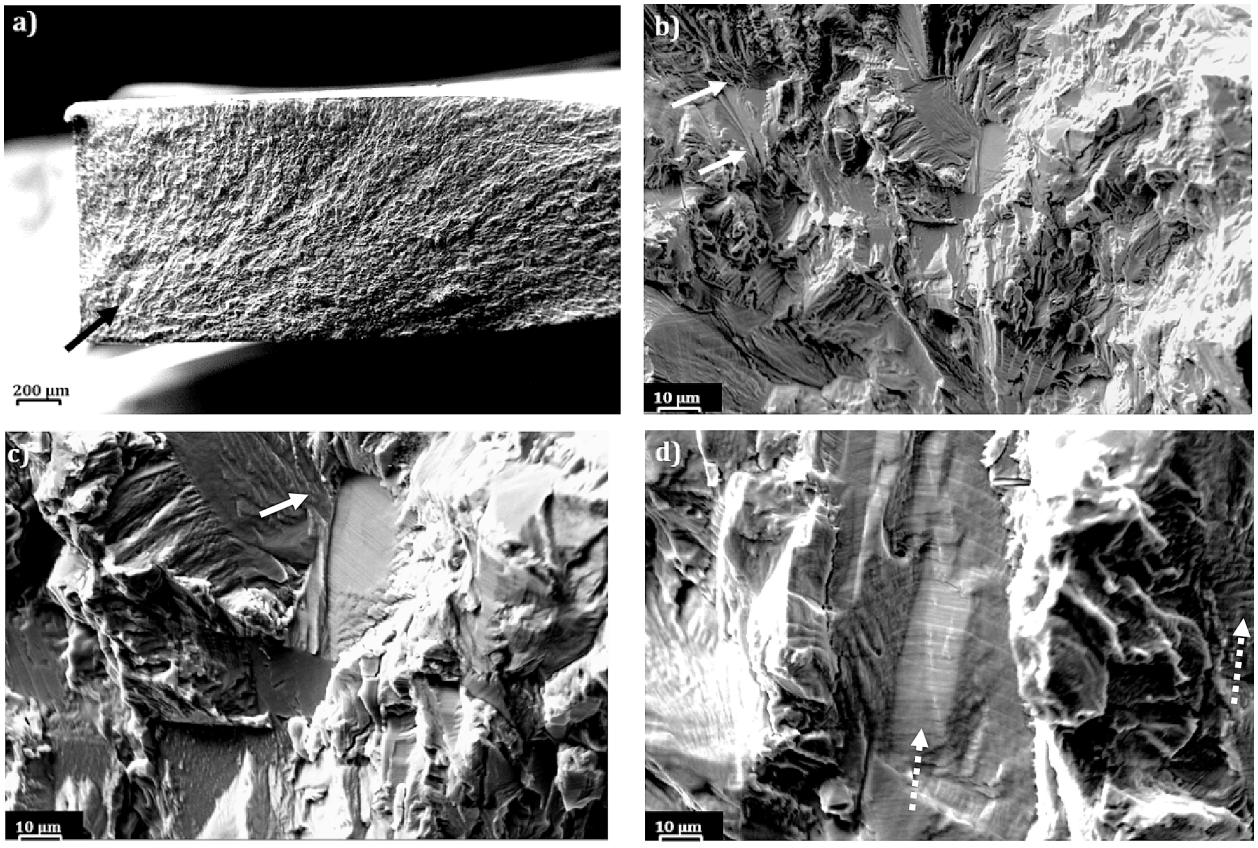

Fig. 7. a) Fatigue crack initiation area of the solution heat treated sample at σ_{max} = 370 MPa; b) Crack initiation on certain crystallographic planes; c) Crack propagation along certain crystallographic planes; d) Fatigue crack striations seen at high magnifications.

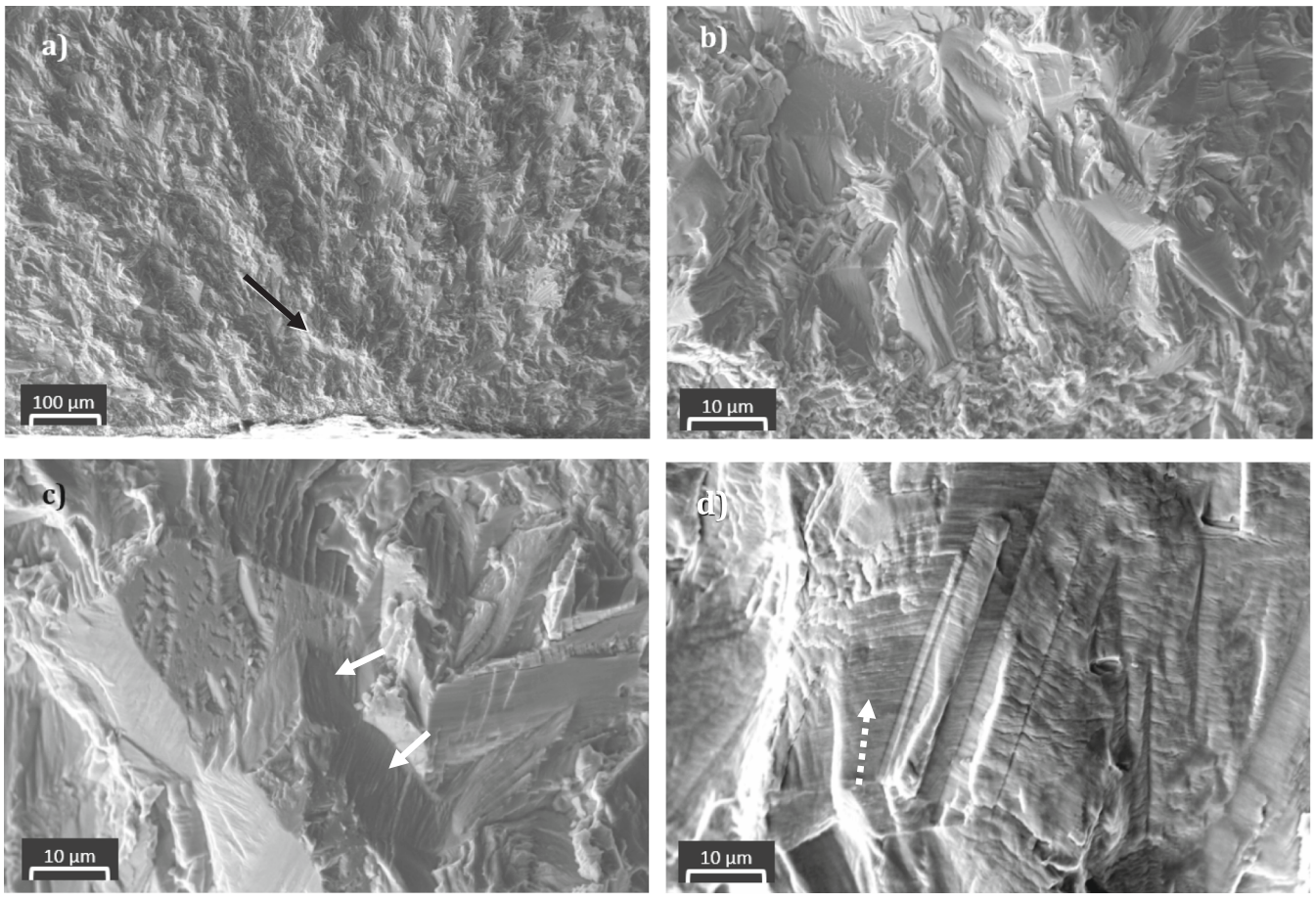

Fig. 8. a) Fatigue crack initiation area of the solution heat treated sample at σ_{max} = 440 MPa; b) Crack initiation on certain crystallographic planes; c) Crack propagation along certain crystallographic planes; d) Fatigue crack striations seen at high magnifications.

stress values higher than 540 MPa, the number of cycles to failure for UA and PA samples tend to overlap. For the solution treated material, the S–N curve becomes horizontal at the maximum stress value of σ_{max} = 360 MPa after 10^7 cycles, which is referred to as the material's fatigue strength σ_f [31]. The highest fatigue strength of 510 MPa is demonstrated by the UA material, whereas the fatigue strength of the PA material is somewhat lower, 460 MPa, but it is still much higher compared to that of the solution heat treated material, 360 MPa. It should be noted that the points on the S-N curves of the studied steels are less scattered than those presented in the literature for multiphase AHSS [32–36]. This observation can be related to the single-phase microstructure of the tested materials. The outcomes of fatigue testing are summarized in Table 1.

3.5. Analysis of fatigue fracture surfaces

After fatigue testing, the fracture surfaces were analyzed by SEM. Areas corresponding to the three stages of fatigue failure (crack initiation, stable crack propagation and sample failure) could be easily identified on all samples [37]. In all studied samples, regardless of the aging condition and applied maximum stress value, the fatigue cracks initiated at the sample surface or subsurface area, and the morphology of the fatigue fracture surfaces looked very similar.

Fig. 7 illustrates the fatigue fracture surface of the solution heat treated sample tested with σ_{max} = 370 MPa. The fatigue crack initiation area is marked by an arrow in Fig. 7a. The fatigue crack was formed by transgranular quasi-cleavage (i.e. through austenite grains) on the surface. It is obvious that the fatigue crack propagated also predominantly by a transgranular mechanism along certain crystallographic planes (Fig. 7c). Fatigue crack striations can be clearly observed on the fatigue crack propagation area (marked by white dashed arrow on Fig. 7d). They represent local crack-growth increments which occur via a mechanism of opening and blunting of the crack tip on loading, followed by resharpening of the tip on unloading [38]. River patterns are also observed (marked by white solid arrows in Fig. 7c). Such patterns develop when a cleavage propagates over a border (a grain or subgrain boundary) between different directions of crystallographic cleavage planes [39]. No significant effect of the stress amplitude on the fatigue crack initiation and propagation mechanisms. Very similar fatigue fracture surface morphology is demonstrated by the solution heat treated sample tested with σ_{max} = 440 MPa (Fig. 8).

The fatigue fracture surfaces of both the UA and PA samples also exhibit a striking resemblance. Fig. 9 presents SEM images of the fatigue fracture surface appearance of the UA sample tested with σ_{max} = 520 MPa. The fatigue crack formed in the subsurface area near the sample corner (Fig. 9a) via a similar mechanism (Fig. 9b) as that observed in the solution-treated material (Fig. 8b). Fatigue crack tends to propagate along certain crystallographic planes leaving river patterns and fatigue crack striations on the surface (Fig. 9b,c). Again, there is no noticeable effect of the stress amplitude on the fatigue crack initiation and propagation mechanisms (Fig. 10). In the peak-aged sample tested with σ_{max} = 470 MPa, the fatigue crack formed near the midsection (Fig. 11a) also via *trans*-granular quasi-cleavage (Fig. 11b). Very well defined fatigue crack striations were also observed on the fatigue crack propagation areas in both cases (Fig. 9c, Fig. 11c). Again, the appearance of the fatigue fracture surfaces was similar in all PA samples independently of the maximum stress value (Fig. 12).

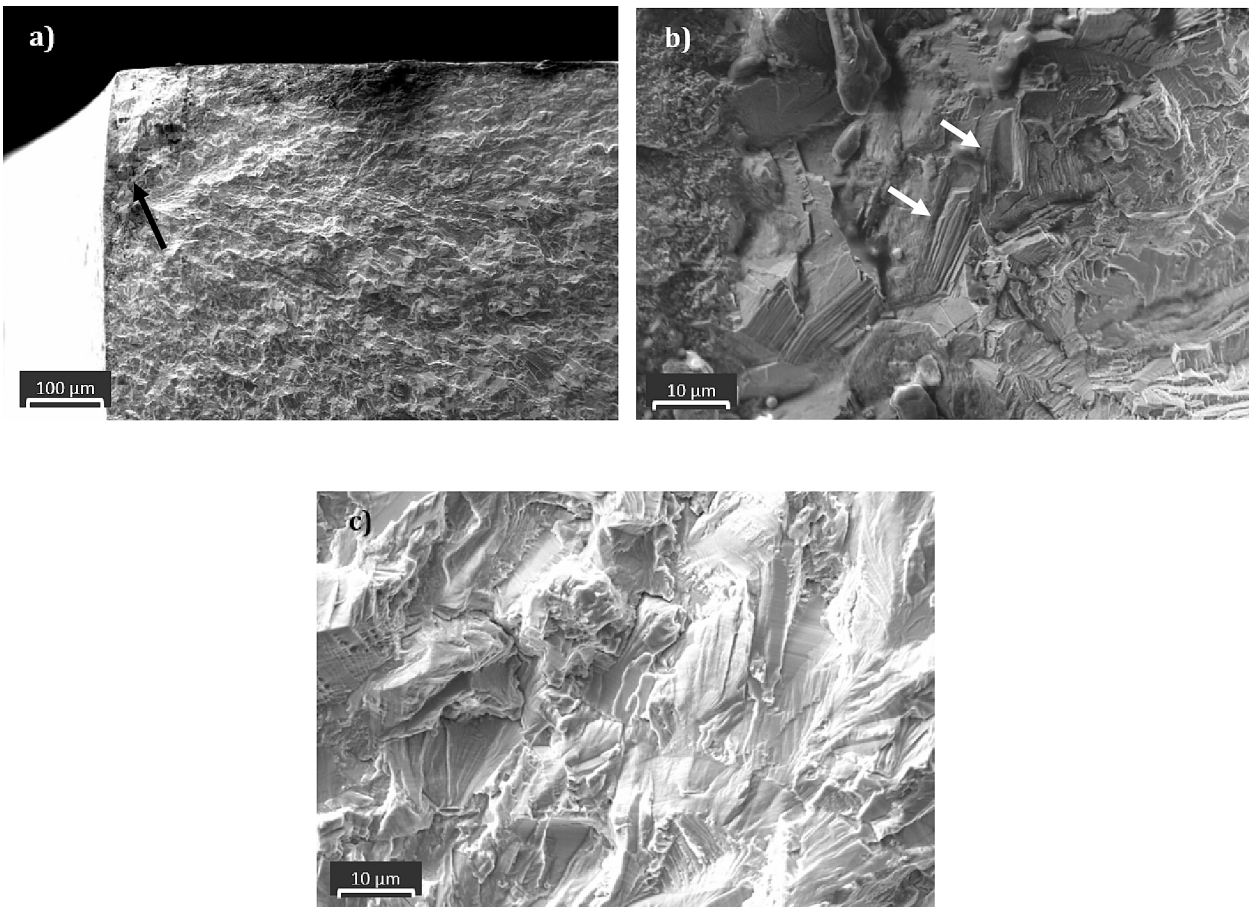

Fig. 9. a) Fatigue crack initiation area of UA sample at σ_{max} = 520 MPa; b) Crack initiation on certain crystallographic planes; c) Crack propagation along certain crystallographic planes.

4. Discussion

4.1. High cycle fatigue performance of the Fe-29Mn-8.7Al-1C steel

The analysis of the S–N curves (Fig. 6) indicates that the best fatigue strength is shown by the UA condition (510 MPa) followed by the PA treatment (460 MPa) and then by the solution treated material (360 MPa). However, another important parameter to be considered is the ratio of fatigue strength to ultimate tensile strength (σ_f/σ_{UTS}). Based on this consideration, the highest σ_f/σ_{UTS} -ratio is demonstrated also by the UA alloy (0.56) followed by the PA alloy (0.43) and then by the solution treated material (0.4) (Table 3).

As is well known, the high-cycle fatigue response of metallic materials is influenced by numerous factors, including fatigue testing parameters, sample quality, and, most importantly, the microstructure of the material. Due to the variability in these parameters, analysing the direct effect of material chemistry, particularly Mn content, on fatigue strength becomes challenging. Nevertheless, a comparison of the high-cycle fatigue behavior of the studied material (Table 3) with that of other high-Mn steels (see Table 4) clearly indicates that the studied Fe-29Mn-8.7Al-1C alloy in the UA condition outperforms all other high-Mn steels reported in the literature [18,23–29]. This is evident in its σ_f/σ_{UTS} ratio of 0.56, which surpasses all other reported values (Table 4). Meanwhile, in the SHT and PA conditions, its high-cycle fatigue response is comparable to or somewhat better than that of the vast majority of the reported materials. Furthermore, the κ-carbides formed during the aging process directly affect the high cycle fatigue behavior of the aged Fe-29Mn-8.7Al-1C alloy and can be employed to control fatigue resistance of the material, as discussed in Section 4.3 below.

4.2. Fatigue crack initiation and propagation

Fatigue crack initiation and propagation play a key role in the fatigue behavior of any metallic material [37]. The fatigue fracture surface analysis clearly shows that fatigue crack initiation and propagation occur by the quasi-cleavage mechanism in all studied conditions (Fig. 8, Fig. 9, Fig. 11). Fig. 13a includes an Euler map obtained from the EBSD analysis of the solution treated alloy with a formed short fatigue crack and a propagating fatigue crack (both in green colour). The black lines correspond to high-angle grain boundaries (>15), and the red line to twin boundaries (~60). The MATLAB analysis [19] of the obtained EBSD data was carried out. TSL software was used to generate the files needed for the MATLAB analysis. The MATLAB program generates a map, where all grains are marked and numbered (Fig. 13c). Furthermore, it is possible to select the grain of interest using the code, which generates all the crystallographic planes of that grain. The grains containing cracks were analysed. Fig. 13b presents a band contrast map with marked crystallographic planes corresponding to fatigue crack propagation planes. It is clearly seen that the fatigue crack forms and propagates in a transgranular manner along [1 1 1] crystallographic planes. There is no evidence of fatigue crack formation at grain or twin boundaries (Fig. 13a). Furthermore, fatigue crack does not tend to propagate along grain or twin boundaries (Fig. 13a). Similar analysis carried out on the other two conditions revealed similar results.

It should be noted that earlier studies revealed that plastic deformation of austenitic Fe-Mn-Al-C alloys occurs by planar glide along [1 1 1] crystallographic planes resulting in the formation of persistent slip bands [40]. Similar mechanism of plastic deformation is observed in the studied material. A TEM image illustrating typical persistent slip bands

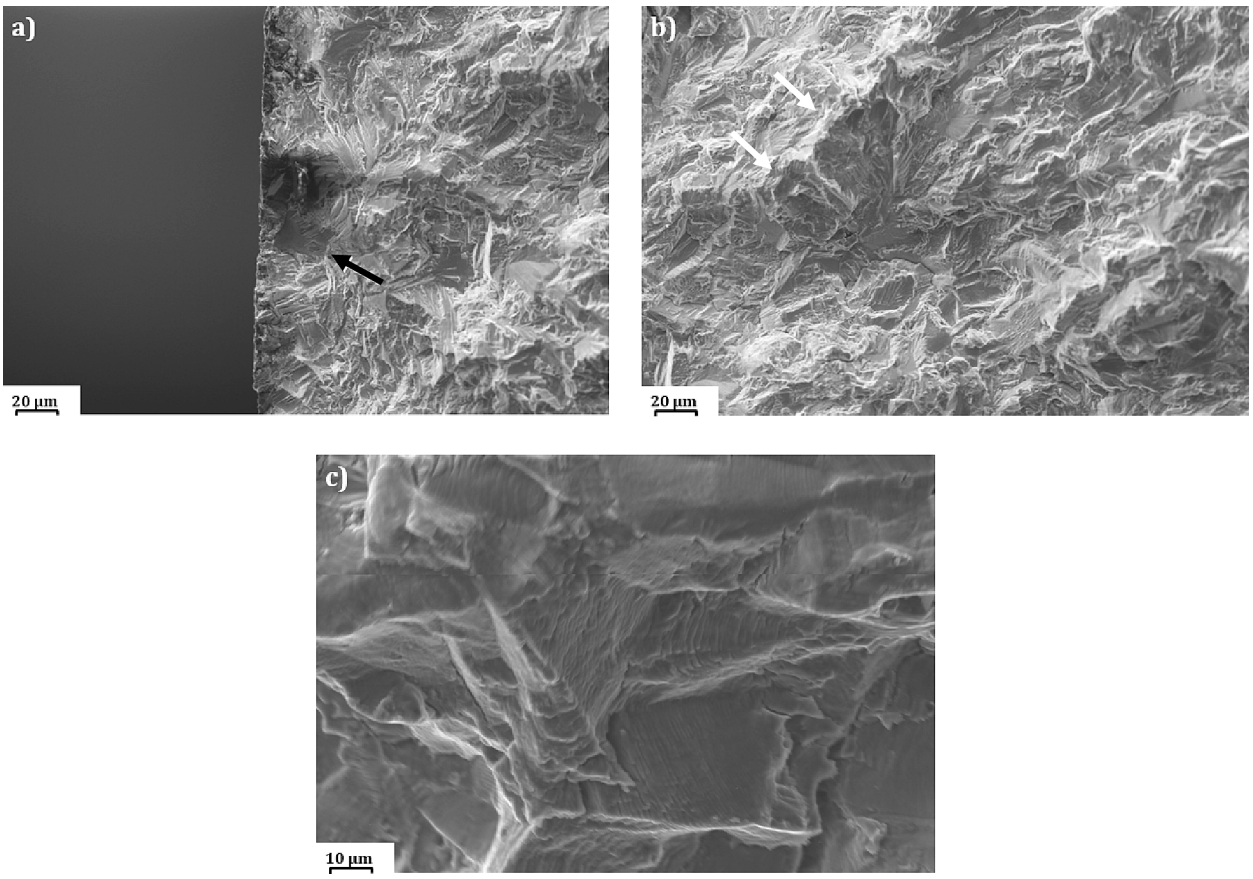

Fig. 10. a) Fatigue crack initiation area of UA sample at $\sigma_{max} = 560$ MPa; b) Crack initiation on certain crystallographic planes; c) Crack propagation along certain crystallographic planes.

developed in the deformed UA alloy is presented in Fig. 14a (marked by white solid arrows). They appear as homogeneously distributed sharp planar zones of high dislocation density having a thickness of 250…300 nm and lying along the activated slip planes [1 1 1]. The distance between bands is in the range of 100…180 μm. Therefore, crack formation and growth along [1 1 1] plane is undoubtedly related to dislocation planar glide. This has been well established for a wide range of metallic materials with fcc lattice, where a similar phenomenon of persistent slip banding was observed, including twinning induced plasticity (TWIP) steels [23,24], austenitic stainless steel [40], Sanicro steel [41], Ni-based superalloys [42,43], copper [44], etc. Experimental studies on austenitic steels revealed that crack-like surface intrusions are the principal mechanism of fatigue crack initiation at persistent slip bands formed in favorably oriented grains during cyclic deformation [38,45]. This mechanism of fatigue crack formation is applicable when the crack emerges on the sample surface. However, there are also cases in which fatigue cracks form in subsurface areas (see, for example, Fig. 11a and Fig. 12a). In these instances, fatigue crack formation at the intersection of persistent slip bands and grain boundaries appears to be the relevant mechanism [23,24]. Once the fatigue crack is formed, the persistent slip band continues to grow ahead of the crack [46] (as can be seen from the kernel average misorientation map on Fig. 13d) paving the way to the transgranular crack propagation. The crack growth path follows the slip band in polycrystals, and the cleavage facets are formed by decohesion along slip planes. Similar fatigue crack propagation mechanism was reported for TWIP steels [23] and austenitic high Mn steels [27,29]. The introduction of κ-carbides into the microstructure of the studied material through artificial aging adds an extra layer of complexity to the fatigue crack initiation and propagation process. This is because the κ-carbides have a significant impact on the motion of dislocations, as discussed in Section 4.3 below.

Evidence of fatigue crack formation at MnS inclusions within the microstructure was not observed. In all analyzed conditions, no inclusions were found in the fatigue crack initiation area of the samples. According to Murakami's analysis [47], the fatigue strength of steels may decrease if the square root of the inclusion's surface area, $\sqrt{area}$, is sufficiently large. For 42CrMo-based steels, the reported critical inclusion size leading to local fatigue crack initiation falls within the range of 8 to 15 μm [48]. Meanwhile, in [49], a range of 10 to 30 μm was proposed for the critical inclusion size. Notably, the MnS inclusions observed in the studied steels are much finer. In addition to inclusion size, the adhesion of inclusions to the matrix is crucial, and in this context, it is worth mentioning that all MnS inclusions were firmly bonded to the austenitic matrix with no debonded interfaces (Fig. 2c).

4.3. The role of κ-carbides in the fatigue behavior of the Fe-29Mn-8.7Al-1C steel

The dislocation – κ-carbide interaction occurs either by Orowan looping of particle shearing [50]. The interaction mechanism is determined by several parameters including particle size, inter-particle distance and antiphase boundary energy (γ_{APB}) [12]. For a lightweight austenitic steel with a very similar chemical composition, Fe-30.4Mn-8Al-1.2C, and antiphase boundary energy of 350 mJ/m^2, it was shown in [12] that the κ-carbides with size less than 10 nm are sheared by gliding dislocations in a weakly coupled regime. Somewhat larger κ-carbides having a size in the range of 10…38 nm are sheared in strongly coupled regime. Orowan looping occurs at even larger κ-carbides (>38 nm). Since the particle size of κ-carbides in this study is less than 10 nm, the predominant regime is the weakly coupled regime, where the gliding dislocations are shearing the κ-carbides resulting in

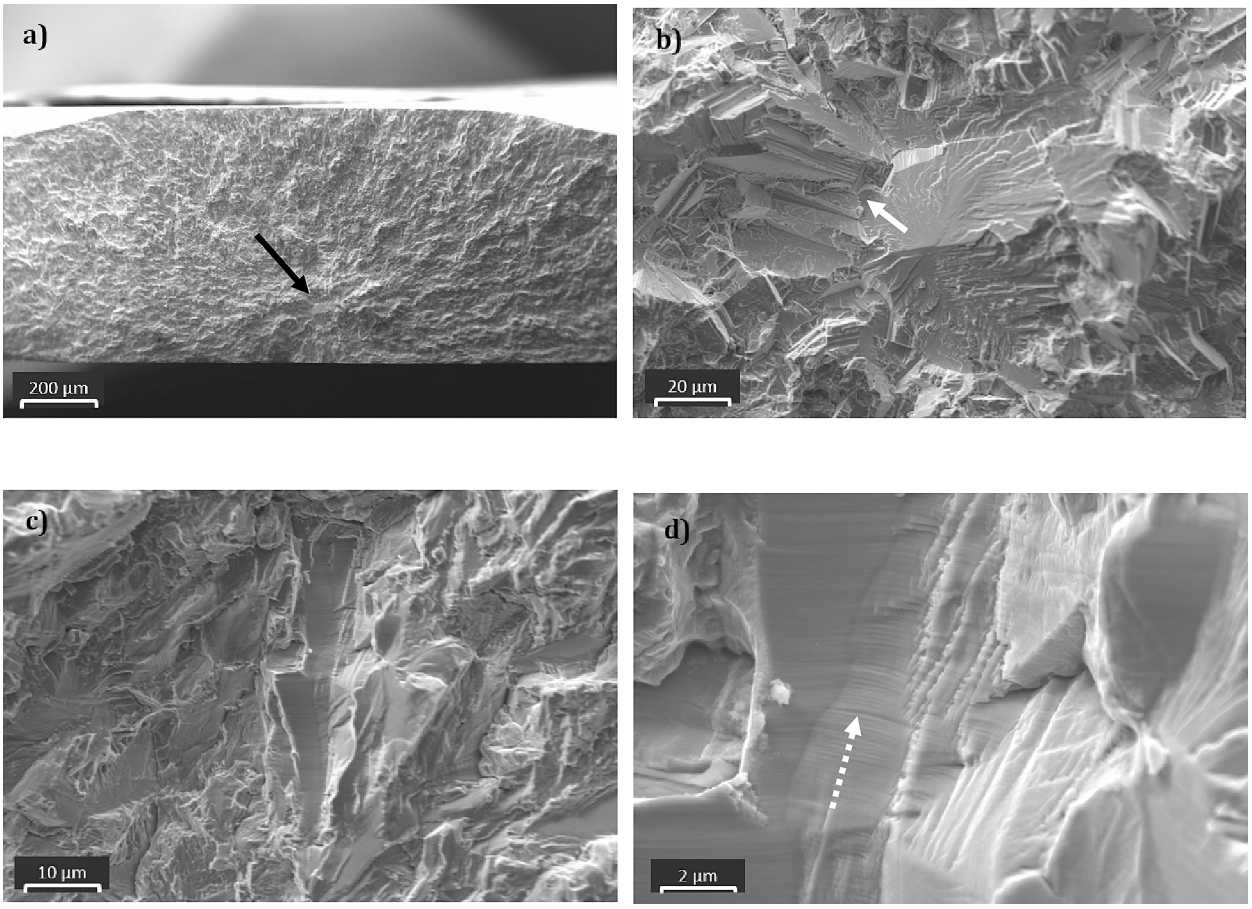

Fig. 11. a) Fatigue crack initiation area of PA sample at σ_{max} = 470 MPa; b) Crack initiation on certain crystallographic planes; c) Crack propagation along certain crystallographic planes; d) Fatigue crack striations at high magnifications.

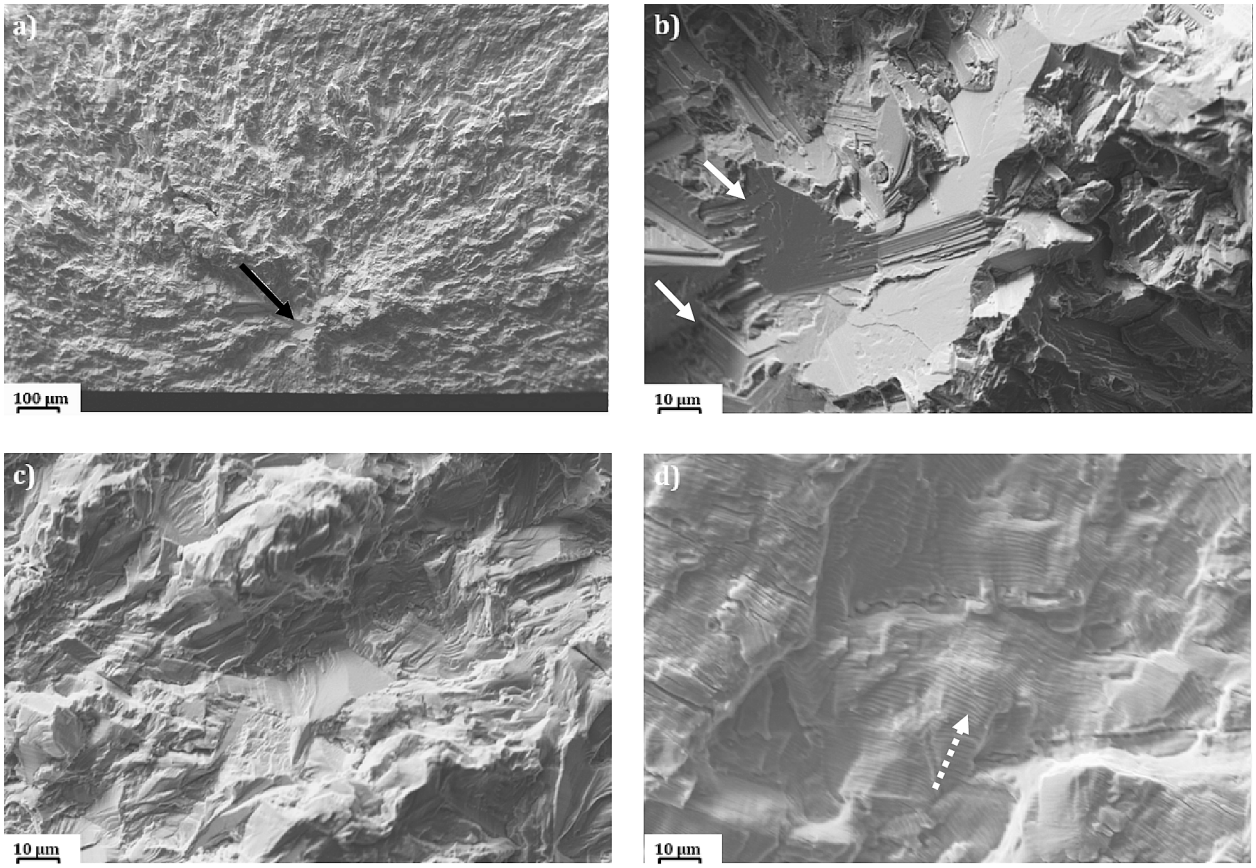

Fig. 12. a) Fatigue crack initiation area of PA sample at $\sigma_{max} = 540$ MPa; b) Crack initiation on certain crystallographic planes; c) Crack propagation along certain crystallographic planes; d) Fatigue crack striations at high magnifications.

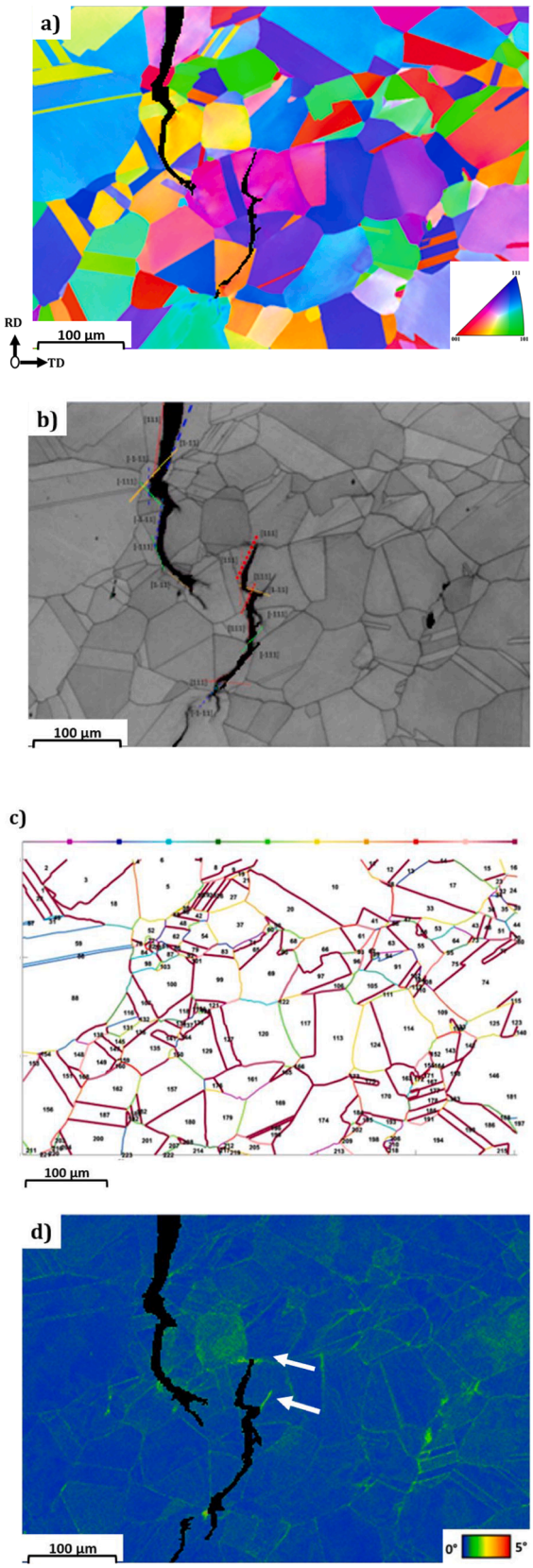

Fig. 13. a) IPF Y map of the solution heat treated material with a formed and a propagating cracks; b) corresponding band contrast map with marked crystallographic planes; c) a map generated by MATLAB software showing all marked grains (the analyzed grains were 5, 52, 85, 98, 100, 107, 134, 120, 127, 161, and 179); d) corresponding kernel average misorientation (KAM) map, calculated for the 3rd neighbour up to 5° misorientation.

the so-called "glide plane softening" [12]. Fig. 14b,c clearly illustrates dislocations cutting κ-carbides in the studied peak-aged material (marked by white solid arrows). Introducing nanoscale κ-carbides into austenitic Fe-Mn-Al-C steels improves the fatigue strength (Table 1, Fig. 6) as formation of persistent slip bands in this case should be delayed due to the additional energy barrier related to the shearing of κ-carbides. Shearing of κ-carbides occurs when the pile-up stress is high enough to overcome the antiphase boundary effect. As mentioned above, the resistance of particles to shearing is determined by an interplay of their size, volume fraction, and antiphase boundary energy [12]. TEM analysis shows that the κ-carbide size and local volume fraction are varying in aged samples [6,7]. Furthermore, the *ab initio* calculations carried out in [12] showed that the antiphase boundary energy is strongly related to the carbon concentration of the κ-carbides, which, in turn, depends on the applied aging treatment parameters. From the results of this study, it is clearly seen that the κ-carbides significantly improve fatigue life when the material is in the under-aged conditions, whereas peak aging somewhat degrades fatigue resistance compared to the under-aged condition. Ab initio calculations of the studied material combined with atom probe tomography studies are needed to further explore the effect of aging treatment on κ-carbide-dislocation interaction during cyclic loading of Fe-29Mn-8.7Al-1C aged samples.

5. Conclusions

The high cycle fatigue behavior of an Fe-29Mn-8.7Al-1C steel was studied in solution heat treated, under-aged, and peak-aged conditions. It was shown that the Fe-29Mn-8.7Al-1C alloy shows a similar or even slightly better fatigue resistance than high Mn alloys with a similar strength, and that the κ-carbides formed during the aging process play a key role in the high cycle fatigue behavior of the Fe-29Mn-8.7Al-1C alloy. In all cases, fatigue crack initiation and propagation occurred predominantly through the quasi-cleavage mechanism along the [1 1 1] crystallographic planes, which is also the preferred plane for planar glide and the formation of persistent slip bands during plastic deformation.

The nanoscale intragranular κ-carbides in the aged samples interact with the gliding dislocations. Based on previous ab-initio results and due to the nanoscale size of the κ-carbides encountered in the studied aging conditions, it is expected that the gliding dislocations induce the shearing of the κ-carbides in the weakly coupled regime. The results show that an optimum aging treatment can significantly improve the fatigue strength of Fe-Mn-Al-C steels, because the formation of persistent slip bands is delayed due to the additional energy barrier associated with the shearing of κ-carbides. The results demonstrate that this improvement peaks at the under-aged condition and that it decreases with further aging time. This behavior can be attributed to the resistance of the κ-particles to shearing, which is determined by their size, volume fraction, and antiphase boundary energy (γ_{APB}), and thus varies during the aging process.

CRediT authorship contribution statement

A. Gomez: Writing – original draft, Visualization, Investigation, Formal analysis, Data curation, Conceptualization. **A. Banis:** Writing – review & editing, Visualization, Supervision, Investigation, Formal analysis, Conceptualization. **M. Avella:** Writing – review & editing, Investigation, Formal analysis, Data curation. **J.M. Molina-Aldareguia:** Writing – review & editing, Validation, Supervision, Resources, Methodology. **R.H. Petrov:** Methodology, Conceptualization, Project administration, Resources, Supervision, Writing – review & editing. **A. Dutta:** Writing – review & editing, Validation, Resources, Project administration. **I. Sabirov:** Writing – review & editing, Supervision, Project administration, Methodology, Funding acquisition, Conceptualization.

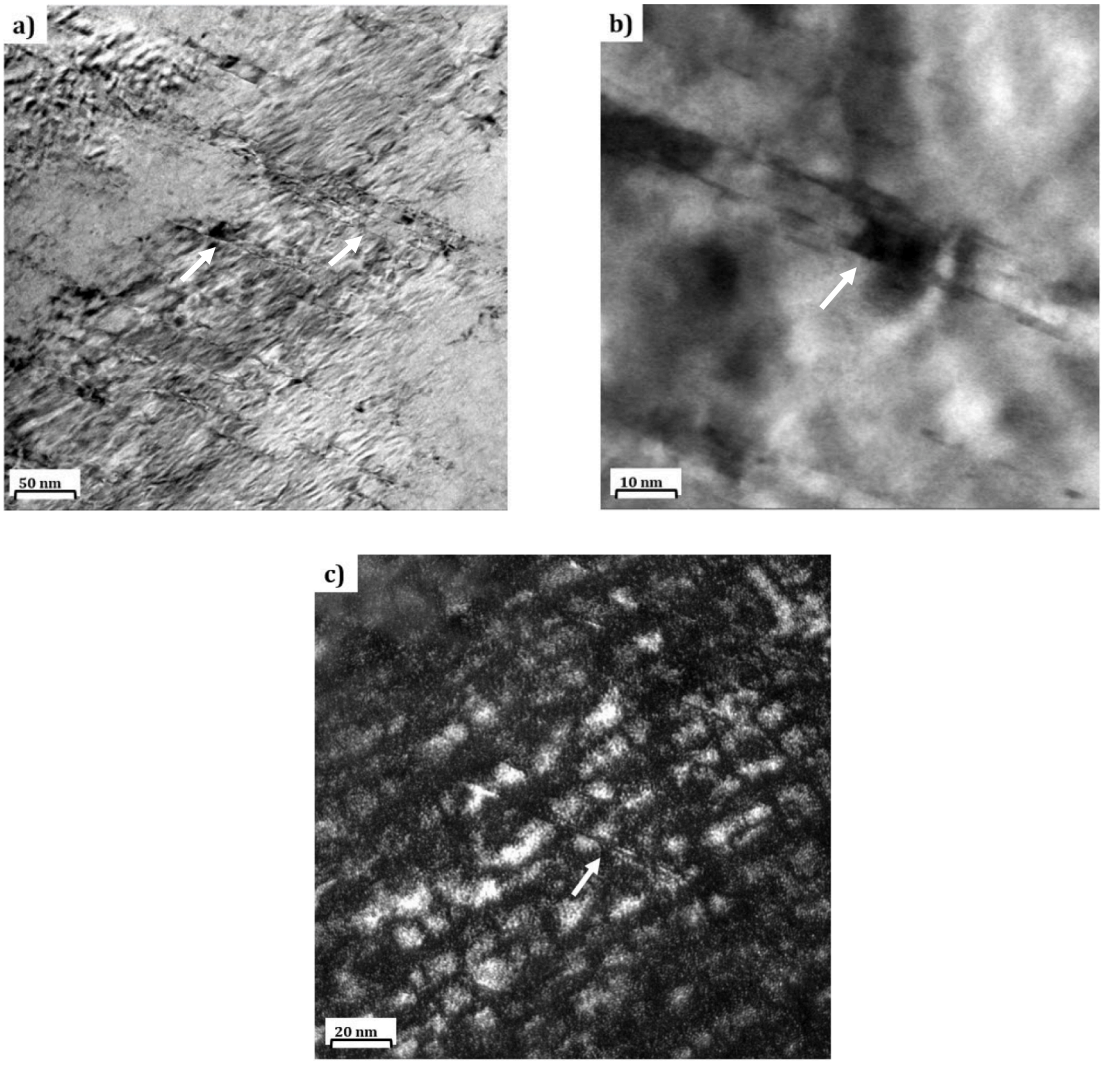

Fig. 14. a) Persistent slip bands in a deformed peak-aged sample (marked by white solid arrows); b) BF TEM image showing κ-carbide being cut by dislocations (marked by a white solid arrow); c) DF TEM image showing dislocation cutting κ-carbides (marked by a white solid arrow).

Declaration of competing interest

The authors declare that they have no known competing financial interests or personal relationships that could have appeared to influence the work reported in this paper.

Data availability

Data will be made available on request.

Acknowledgements

The authors would like to acknowledge financial support from the Research Fund for Coal and Steel (RFCS) of the European Union via the DELIGHTED project (Grant No. 899332).

References

[1] Chen S, Rana R, Haldar A, Ray RK. Current state of Fe-Mn-Al-C low density steels. Prog Mater Sci 2017;89:345–91.
[2] H. Kim, D.W. Suh, N.J. Kim. Fe–Al–Mn–C lightweight structural alloys: a review on the microstructures and mechanical properties. Sci. Tech. Adv. Mater. 14 (2013) 1-11. 3.
[3] Zambrano OA. A general perspective of Fe-Mn-Al-C steels. J Mater Sci 2018;53:14003–62.
[4] Ding H, Liu D, Cai M, Zhang Y. Austenite-based Fe-Mn-Al-C lightweight steels: Research and prospective. Metals 2022;12:1572.
[5] Liu DG, Cai MH, Ding H, Han D. Control of inter/intra-granular κ-carbides and its influence on overall mechanical properties of a Fe-11Mn-10Al-1.25C low density steel. Mater Sci Eng A 2018;715:25–32.
[6] Banis A, Gomez A, Bliznuk V, Dutta A, Sabirov I, Petrov RH. Microstructure evolution and mechanical behavior of Fe–Mn–Al–C low-density steel upon aging. Mater Sci Eng A 2023;875:145109.
[7] Banis A, Gomez A, Dutta A, Sabirov I, Petrov RH. The effect of nano-sized κ-carbides on the mechanical properties of an Fe-Mn-Al-C alloy. Mater Charact 2023;205:113364.
[8] Liu DG, Ding H, Cai MH, Han D. Mechanical behaviors of a lower-Mn-added Fe-11Mn-10Al-1.25C lightweight steel with distinguished microstructural features. Mater Lett 2019;242:131–4.
[9] Liu DG, Ding H, Han D, Cai MH, Lee YK. Microstructural evolution and tensile properties of Fe-11Mn-10Al-1.2C medium-mn lightweight steel. Mater Sci Eng A 2020;797:140256.
[10] Haase C, Zehnder C, Ingendahl T, Bikar A, Tang F, Hallstedt B, et al. On the deformation behavior of κ-carbide-free and κ-carbide-containing high-Mn lightweight steel. Acta Mater 2017;122:332–43.
[11] Kim SD, Park SJ, Jang J, Moon JH, Ha HY, Lee CH, et al. Strain hardening recovery mediated by coherent precipitates in lightweight steel. Sci Rep 2021;11:14468.
[12] Yao MJ, Welsch E, Ponge D, Haghighat SMH, Sandlobes S, Choi P, et al. Strengthening and strain hardening mechanisms in a precipitation-hardened high-Mn lightweight steel. Acta Mater 2017;140:258–73.
[13] Lee S, Kang SH, Nam JH, Lee SM, Seol JB, Lee YK. Effect of Tempering on the microstructure and tensile properties of a Martensitic medium-Mn lightweight steel. Metall Mater Trans 2019;50A:2655–64.
[14] Chang SC, Hsiau YH, Jahn MT. Tensile and fatigue properties of Fe-Mn-Al-C alloys. J Mater Sci 1989;24:1117–20.

[15] Ho NJ, Tjong SC. Cyclic stress-strain behaviour of austenitic Fe-29.7Mn-8.7Al-1.04C (wt. %) alloy at room temperature. Mater Sci Eng A 1987;94:195–202.
[16] Kalashnikov IS, Acselrad O, Pereira LC, Kalichak T, Khadyyev MS. Behavior of Fe-Mn-Al-C steels during cyclic tests. J Mater Eng Perform 2000;9:334–7.
[17] Wegener T, Haase C, Liehr A, Niendorf T. On the influence of κ-carbides on the low-cycle fatigue behavior of high-Mn light-weight steels. Int J Fatig 2021;150:106327.
[18] Seo W, Jeong D, Sung H, Kim S. Tensile and high cycle fatigue behaviors of high-Mn steels at 298 and 110K. Mater Charact 2017;124:65–72.
[19] Bieler TR, Eisenlohr P, Zhang C, Phukan HJ, Crimp MA. Grain boundaries and interfaces in slip transfer. Curr Opin Solid State Mater Sci 2014;18:212–26.
[20] ASTM E8 / E8M-09. Standard Test Methods for Tension Testing of Metallic Materials, ASTM International.
[21] International Organization for Standardization ISO 1099:2006(E) 2006 Metallic materials-Fatigue testing-Axial force controlled method Geneva, Switzerland.
[22] Park JH, Kim DJ, Min DJ. Characterization of Nonmetallic inclusions in high-manganese and aluminum-alloyed austenitic steels. Metall Mater Trans A 2012;43:2316–24.
[23] Hamada AS, Karjalainen LP, Puustinen J. Fatigue behavior of high-Mn TWIP steels. Mater Sci Eng A 2009;517:68–77.
[24] Hamada AS, Karjalainen LP, Ferraiuolo A, Gil Sevillano J, De Las Cuevas F, Pratolongo G, et al. Fatigue behavior of four high-Mn twinning induced plasticity effect steels. Metall Mater Trans A 2010;41:1102–8.
[25] Sung HK, Jeong DH, Park TD, Lee JS, Kim SS. SN fatigue behavior of Fe25Mn steel and its weld at 298 and 110 K. Metal Mater Inter 2016;22:755–63.
[26] Jeong DH, Park TD, Lee JS, Kim SS. Ambient and cryogenic SN fatigue behavior of Fe15Mn steel and its weld. Metal Mater Inter 2015;21:453–60.
[27] Jeong DH, Lee SG, Jang WK, Choi JK, Kim YJ, Kim SS. Cryogenic S-N fatigue and fatigue crack propagation behaviors of high manganese austenitic steels. Metall Mater Trans A 2013;44:4601–12.
[28] Wang B, Zang P, Duan QQ, Zhang ZJ, Yang HJ, Zhang ZF. High-cycle fatigue properties and damage mechanisms of pre-strained Fe-30Mn-0.9C twinning-induced plasticity steel. Mat Sci Eng A 2017;679:258–71.
[29] Kim SS, Kwon JK, Kim YJ, Jang WK, Lee SG, Choi JK. Factors influencing fatigue crack propagation behavior of austenitic steels. Met Mater Int 2013;19:683–90.
[30] Zhang P, Li SX, Zhang ZF. General relationship between strength and hardness. Mater Sci Eng A 2011;529:62–73.
[31] Dieter GE. Mechanical metallurgy. New York: McGraw-Hill; 1976.
[32] Sierra-Soraluce A, Li G, Santofimia MJ, Molina-Aldareguia JM, Smith A, Muratori M, et al. Exploring the effect of complex hierarchic microstructure of quenched and partitioned martensitic stainless steels on their high cycle fatigue behaviour. Mater Des 2023;233:112286.
[33] Haidemenopoulos GN, Kermanidis AT, Malliaros C, Dickert HH, Kucharzyk P, Bleck W. On the effect of austenite stability on high cycle fatigue of TRIP 700 steel. Mater Sci Eng A 2013;573:7–11.
[34] de Diego-Calderón I, Rodriguez-Calvillo P, Lara A, Molina-Aldareguia JM, Petrov RH, De Knijf D, et al. Effect of microstructure on fatigue behavior of advanced high strength steels produced by quenching and partitioning and the role of retained austenite. Mater Sci Eng A 2015;641:215–24.
[35] Hao Q, Zhou Q, Yang Q, Zhang K, Yang W, Zheng C, et al. Effects of retained austenite and softened martensite on high-cycle fatigue behavior of spring steel under two loading modes. Steel Res Int 2023;94:2200399.
[36] Abareshi M, Emadoddin E. Effect of retained austenite characteristics on fatigue behavior and tensile properties of transformation induced plasticity steel. Mater Des 2011;32:5099–105.
[37] Suresh S. Fatigue of materials. Cambridge: Cambridge University Press; 1998.
[38] Hull D. Fractography: observing, measuring and interpreting fracture structure topography. Cambridge University Press; 1999.
[39] Bertram Broberg K. Cracks and Fracture. Academic Press 1999:5–26.
[40] Mazanova V, Skorik V, Kruml T, Polak J. Cyclic response and early damage evolution in multiaxial cyclic loading of 316L austenitic steel. Int J Fatigue 2017;100:466–76.
[41] Polak J, Petras R, Chai GC, Skorik V. Surface profile evolution and fatigue crack initiation in sanicro 25 steel at room temperature. Mater Sci Eng A 2016;658:221–8.
[42] Healy JC, Grabowski L, Beevers CJ. Short-fatigue-crack growth in a nickel-base superalloy at room and elevated temperature. Int J Fatigue 1991;13:133–8.
[43] Antolovich SD. Microstructural aspects of fatigue in Ni-based superalloys. Phil Trans A 2015;373:20140128.
[44] Hoppel HW, Goik P, Krechel C, Goken M. Ex and in situ investigations on the role of persistent slip bands and grain boundaries in fatigue crack initiation. J Mater Res 2017;32:4276–86.
[45] Polak J, Mazanova V, Heczko M, Kubena I, Man J. Profiles of persistent slip markings and internal structure of underlying persistent slip bands. Fatig Fract Eng Mater Struct 2017;40:1101–16.
[46] Lukas P, Kunz L. Role of persistent slip bands in fatigue. Phil Mag 2004;84:317–30.
[47] Murakami H. Metal fatigue: effects of small defects and Nonmetallic inclusions. Elsevier; 2002.
[48] Yang ZG, Yao G, Li GY, Li SX, Chu ZM, Hui WJ, et al. The effect of inclusions on the fatigue behavior of fine-grained high strength 42CrMoVNb steel. Int J Fatig 2004;26:959–66.
[49] Findley KO, Cryderman RL, Nissan AB, Matlock DK. The effect of inclusions on fatigue performance of steel alloys. AIST Trans 2013;10:234–43.
[50] Martin JW. Precipitation hardening. Oxford, UK: Butterworth-Heinemann; 1998.